Analyst

PAPER

View Article Online
View Journal | View Issue

Cite this: *Analyst*, 2014, **139**, 416

New insight into protein–nanomaterial interactions with UV-visible spectroscopy and chemometrics: human serum albumin and silver nanoparticles†

Yong Wang[a] and Yongnian Ni*[ab]

Received 24th September 2013
Accepted 29th October 2013

DOI: 10.1039/c3an01818k

www.rsc.org/analyst

In recent years, great efforts have focused on the exploration and fabrication of protein nanoconjugates due to potential applications in many fields including bioanalytical science, biosensors, biocatalysis, biofuel cells and bio-based nanodevices. An important aspect of our understanding of protein nanoconjugates is to quantitatively understand how proteins interact with nanomaterials. In this report, human serum albumin (HSA) and citrate-coated silver nanoparticles (AgNPs) are selected as a case study of protein–nanomaterial interactions. UV-visible spectroscopy together with multivariate curve resolution by alternating least squares (MCR-ALS) algorithm is first exploited for the detailed study of AgNPs–HSA interactions. Introduction of the chemometrics tool allows extracting the kinetic profiles, spectra and distribution diagrams of two major absorbing pure species (AgNPs and AgNPs–HSA conjugate). These resolved profiles are then analysed to give the thermodynamic, kinetic and structural information of HSA binding to AgNPs. Transmission electron microscopy, circular dichroism spectroscopy and Fourier transform infrared spectroscopy are used to further characterize the complex system. Moreover, a sensitive spectroscopic biosensor for HSA is fabricated with the MCR-ALS resolved concentration of absorbing pure species. It is found that the linear range for the HSA nanosensor was from 1.9 nM to 45.0 nM with a detection limit of 0.9 nM. It is believed that the proposed method will play an important role in the fabrication and optimization of a robust nanobiosensor or cross-reactive sensors array for the detection and identification of biocomponents.

Introduction

Research at the interface of nano and biological sciences offers the promise to drive revolutionary advances in basic and applied science and technology.[1–3] In the past few years, the research focus has been mainly on bionanoconjugates that combine the properties of nanomaterials with the functions of biomolecules.[4–6] Proteins are large biological molecules that possess many unique biochemical properties and which have attracted worldwide research interest since their discovery.[7] The design and generation of protein–nanomaterial conjugates have recently presented a highly attractive platform for a variety of novel practical applications in the area of bioanalysis,[8–10] biosensing,[11,12] biocatalysis[13,14] and molecular electronic devices.[15,16] A key challenge in understanding protein–nanomaterial conjugates is to probe the interactions of proteins with nanomaterials, or rather, to investigate kinetic, thermodynamic, and structural information on protein–nanomaterial interactions.[17]

Presently, many analytical techniques and strategies[18–21] like analytical ultracentrifugation, dynamic light scattering, small-angle scattering, atomic force microscopy, circular dichroism spectroscopy, nuclear magnetic resonance, quartz crystal microbalance, surface plasmon resonance and calorimetry, have been reported to permit the study of these interactions. Despite the importance and the success of these methods, most of them cannot simultaneously provide information about the thermodynamics, kinetics and structure related to protein–nanomaterial interactions. Hence, it is imperative to explore an appealing alternative to characterize the interactions between proteins and nanomaterials in a systematic manner.

Owing to ease of operation and low cost, UV-visible spectroscopy is routinely used in the characterization of protein-conjugated nanomaterials. At present, almost all the literature pays attention only to the effect of proteins binding to nanomaterials.[20–23] Researchers find that the binding of protein to nanomaterials results in some changes in the UV-visible absorption spectra, such as the small spectral shift, slight spectral widening and tiny spectral intensity alterations.[20–23]

Analysis of the spectral changes is usually performed in a univariate manner, and thus it is difficult to gain more

[a]*Department of Chemistry, Nanchang University, Nanchang 330031, China. E-mail: ynni@ncu.edu.cn; Fax: +86 791 83969500; Tel: +86 791 83969500*

[b]*State Key Laboratory of Food Science and Technology, Nanchang University, Nanchang 330047, China*

† Electronic supplementary information (ESI) available. See DOI: 10.1039/c3an01818k

quantitative information on the protein–nanomaterial interactions. Moreover, subtle spectral changes and serious spectral overlap among coexisting absorbing species also hinder a deep analysis of spectral data from multivariate measurements. As a result, there is an ongoing need for a new and effective analytical tool to extract underlying information on protein binding to nanomaterials quantitatively.

During the last few years, chemometrics has gained increasing popularity in the analysis of macromolecules, nanomaterials or their combinations.[24–32] Among them, the multivariate curve resolution with alternating least squares (MCR-ALS) algorithm developed by Tauler *et al.*[32] is very likely to be the most powerful chemometrics approach used for the resolution of multiple component responses in unknown unresolved mixtures because the method need not conform to a rigorous multilinear model, which allows the application of other more hard model decomposition algorithms, for example parallel factor analysis (PARAFAC).[33] As a matter of fact, the data matrices under spectral analysis usually hardly meets the requirement of a multilinear structure mainly due to spectral distortions, experimental noise and a high spectral or concentration colinearity. At present, UV-visible spectroscopy together with the MCR-ALS tool has been successfully applied for detailed interpretation of complex systems containing proteins or nanomaterials, but there are almost no literature reports of their application for the study of protein-conjugated nanomaterials.[34–37]

In the present report, we explored the use of UV-visible spectroscopy for the study of the evolutionary process of protein–nanomaterials conjugate, and exploited the powerful resolution advantage of multivariate data analysis tool, MCR-ALS, to gain a new insight into protein–nanomaterial interactions. The application of MCR-ALS allows qualitative and quantitative recovery of the distribution diagrams, spectra and kinetic profiles of the absorbing pure species. The response profiles recovered can be further translated into thermodynamic, kinetic and structural parameters describing protein binding to nanomaterials. We herein take citrate-coated silver nanoparticles (AgNPs) and human serum albumin (HSA) as a prototype. AgNPs possess sufficiently high and long-lasting antimicrobial activity against a range of gram positive and gram negative bacteria, and thus have been used for many years in consumer products, cosmetics, medical products and medical therapy.[38] Furthermore, because the AgNPs preparation methods are well established and AgNPs possess good optical and electronic properties, they are widely applied for the fabrication of biosensors.[39] HSA is the most abundant protein found in blood plasma, its three-dimensional shape (HSA has a triangular prism-shaped structure with the dimensions of 8.4 nm × 8.4 nm × 3.15 nm)[40] has been well-studied. Simultaneously, we also employed AgNPs as optical probes to develop a nanobiosensor for HSA detection with high sensitivity.

Experimental

Instrumentation and software

UV-visible spectra were measured with an Agilent 8453 UV-visible spectrometer attached with a Model ZC-10 (Ningbo Tianheng Instruments Factory, China) temperature control accessory in a rectangular quartz cuvette of 10 mm path length. Circular dichroism spectral (CD) measurements were taken with a Bio-Logic MOS 450 spectropolarimeter (Bio-Logic, France) using a 1.0 mm path length quartz cuvette. Transmission electron microscopy (TEM) was conducted with a JEM-2010 transmission electron microscope operated at an accelerating voltage of 200 kV. Samples for TEM characterization were suspended in water and sonicated for three minutes. Then, a drop of colloidal solution was transferred onto porous carbon foils supported on copper microgrids. Fourier transform infrared spectroscopy (FT-IR) scans were collected in the transmission mode with IR grade KBr as the scanning matrix on a Nicolet 380 FT-IR spectrometer (Thermo Nicolet Corporation, USA) equipped with a DTGS KBr detector and a KBr beam splitter. Samples for FT-IR characterization were prepared by placing 5 μL of HSA or colloidal solution on KBr pellets. Then, the samples were evaporated to remove water.

All MCR-ALS calculations were made using in-house in MATLAB 7.0 (Mathworks) routines freely downloaded from the web page "http://www.cid.csic.es/homes/rtaqam/tmp/WEB_MCR/welcome.htm". A detailed explanation of the MCR-ALS algorithm for the research of protein–nanomaterial interactions are included in the ESI.†

Reagents and chemicals

Trisodium citrate dihydrate and silver nitrate were obtained from Shanghai Chemical Reagent Co. (Shanghai, China). Human serum albumin (HSA) was purchased from Solarbio Science & Technology Co., Ltd. (Beijing, China). Unless specified, all chemicals were analytical-reagent grade and used without further treatment. Double distilled water was used in all preparations. Prior to use, a stock solution of HSA (1.0×10^{-3} M) was prepared by dissolving 0.3323 g of the purified protein ($M_w = 66\,450$ Da) in 5.0 mL water and stored in a refrigerator at 4 °C. Its accurate concentration was determined spectrophotometrically using the molar absorptivity value at 278 nm ($\varepsilon_{HSA} = 3.44 \times 10^4$ M^{-1} cm^{-1}).[41]

Preparation of AgNPs

All glassware was cleaned with freshly prepared aqua regia followed by water. Citrate-coated AgNPs were prepared according to the previously reported procedure with minor modifications.[42] Briefly, 18 mg of silver nitrate was dissolved in 100 mL water and mixing thoroughly. The solution was brought to boiling with rapid stirring. Thereafter, to this solution was rapidly added 10 mL of 1% trisodium citrate. The color of the solution slowly turned grayish yellow. After boiling for 1 h, the solution was removed from the heating source, and stirring continued for an additional 30 min. The solution was then allowed to cool naturally to room temperature. Finally, the solution was diluted with water to give a final volume of 100 mL. The pH value of the citrate-coated AgNPs solution was determined to be about 7.3. The TEM image of the AgNPs (see Fig. S1 ESI†) showed nearly spherical particles of diameter 38.6 ± 12.9 nm (the size of AgNPs was measured based on more than

300 nanoparticles). The extinction coefficient, ε, of AgNPs at peak wavelength (412 nm) can be calculated to be 3.31×10^{10} M^{-1} cm^{-1} based on the following equation $\ln \varepsilon = 1.4418 \ln D + 18.955$ (D is the diameter of AgNPs in nm),[43] and thus the concentration of AgNPs was determined to be 0.0221 nM by UV-visible spectroscopy.

UV-visible spectral measurements for the HSA–AgNPs interaction study

For the study of the interactions between HSA and AgNPs, the selected volume (x μL) of water and 165 μL of AgNPs solution (pH 7.3) were micropipetted into a 3.5 mL cuvette. The solution in the cuvette was stirred by auto-controlled micro-stirring and kept for 2 min in the controlled-temperature cuvette holder. Then, an aliquot of $(1835 - x)$ μL of 7.5 μM HSA solution was rapidly added to give a series of samples with different concentrations (range: $c_{HSA} = 0$–75.0 nM; total: 13 samples). All time-dependent spectra were followed simultaneously from 240 nm to 700 nm, every 1 nm, at 2.5 s intervals during 60 s with respect to water as a blank. All experiments were carried out at three constant temperatures (298.15 K, 303.15 K and 308.15 K).

Theoretical background for the MCR-ALS algorithm

The MCR-ALS algorithm developed by Tauler *et al.*[32] is a powerful chemometrics approach used for the resolution of multiple component responses in unknown unresolved mixtures. It decomposes the original mixture bidimensional data matrix, **D**, into the product of two submatrices, **C** and $\mathbf{S}^T$, which contain the pure profiles of all the chemical contributions, plus the residual or error data matrix, **E**, related to unexplained data variance. The decomposition process of the general MCR-ALS bilinear model can be given as:

$$\mathbf{D} = \mathbf{C}\,\mathbf{S}^T + \mathbf{E} \quad (1)$$

In the context of time-dependent UV-visible absorption spectral measurement of a complex chemical system, the experimental data matrix, **D**, contains the mixed spectra registered along specified time dimension. The submatrices, **C** and $\mathbf{S}^T$ have the resolved kinetic and spectral information about the contributions of pure components in the chemical evolving process. Superscript T represents the transpose of a matrix.

The mathematical model follows three steps. Firstly, the number of pure components that independently contribute to the measured absorbance in the matrix **D** is determined. This can be usually determined by a singular value decomposition[33] or the theory of error in factor analysis.[44] Secondly, an initial estimate of concentration evolution profiles, **C**, or spectra, $\mathbf{S}^T$, of the pure component present in the matrix **D** is built up. The initial estimate of their concentration evolution or spectral profiles can be often be obtained using either chemometrics methods such as classical evolving factor analysis (EFA) and simple-to-use interactive self-modelling mixture analysis (SIMPLISMA) or previous knowledge of the chemical system under investigation.[33] Thirdly, the resolution of the pure profiles of all the chemical contributions can be given by an iterative ALS algorithm.

Generally, the results the MCR-ALS method yielded are subject to rotational and intensity ambiguities if no assumptions are made at all about the possible values and shapes of the concentration evolution and spectral profiles of the modelled components.[33] As a result, some constraints that reflect the chemical nature and intrinsic mathematical structure of the studied system are always introduced to the iterative calculations of **C** and $\mathbf{S}^T$. Some main constraints are non-negativity (the response takes positive values), unimodality (the presence of one maximum per profile), closure (the sum of concentrations of the different species is constant), local rank information (some species known to be absent are set to zero) and component correspondence (the common species in the different samples is identified).[33]

In addition, the MCR-ALS method is also applied to study several experiments monitored with the same technique simultaneously, the same experiment monitored with different techniques, or different experiments monitored with different techniques, showing it has an important advantage for data fusion analysis. The multiple independent data sets given by different processes can be concatenated along the specified direction to generate column-wise augmented data matrix (the same technique is used under different experimental conditions), row-wise augmented data matrix (the same experiment is used under different techniques) and row- and column-wise augmented data matrix. The general steps of the algorithm for data fusion analysis are those explained above. Constraints can be individually or simultaneously used to each **C** and $\mathbf{S}^T$ submatrices.

The convergence criterion in the MCR-ALS optimization is based on the comparison of the standard deviations of the residuals between the experimental and the MCR-ALS reproduced data in two consecutive iterations. When the relative differences in the standard deviations are below a threshold value, the optimization is stopped. The quality of the MCR-ALS model is assessed by three indicators, *i.e.*, the percentage of lack of fit (LOF), the percentage of explained variance (R^2), and the similarity coefficient (r). They are defined as follows:[33]

$$\mathrm{LOF}\ (\%) = 100 \times \sqrt{\frac{\sum_{i,j} e_{ij}^2}{\sum_{i,j} d_{ij}^2}} \quad (2)$$

$$R^2\ (\%) = 100 \times \left(1 - \frac{\sum_{i,j} e_{ij}^2}{\sum_{i,j} d_{ij}^2}\right) \quad (3)$$

$$r = \cos\gamma = \frac{x_i^T \hat{x}_i}{\|x_i^T\| \times \|\hat{x}\|} \quad (4)$$

where e_{ij} and d_{ij} represent the residual given by difference between the input element and the reproduction from $\mathbf{CS}^T$ product estimated using the MCR-ALS method, and an element of the input data matrix **D**. Subscripts i and j denote the rows

and columns of the original data matrix, respectively. γ refers to the angle of the vectors associated with the MCR-ALS resolved profile ($\hat{x}_i$) and the true pure profile (x_i), for a certain species.

Overall, a good modelling fit of the experimental data is available when the values of LOF, R^2 and r approach zero, one, and one, respectively.

MCR-ALS analysis for protein–nanomaterial interactions

In this report, to systematically probe protein–nanomaterial interaction, time-dependent UV-visible spectra for m samples at constant temperature were collected by keeping the concentration of the nanomaterial constant and changing the concentration of protein. As can be showed in Scheme 1, for each experiment, the time-dependent spectra containing mixed information are arranged in a data matrix of $\mathbf{D}_m$ (size $t \times w$), with as many t rows as number of recorded spectra at each measured time point and as many w columns as the number of kinetic profiles scanned at each specified wavelength. Each independent data set related to the m mole-ratio experiments, $\mathbf{D}_1$, $\mathbf{D}_2$, $\mathbf{D}_3 \ldots \mathbf{D}_m$, can be arranged as a new column-wise augmented matrix of size $(t \times m) \times w$, $\mathbf{D}_{aug}$. The m mole-ratio experiments were run under the same condition, and hence there are identical spectra for the same absorbing pure components in each experiment. Mathematically, this suggests that in this matrix augmentation, common vectors span the column vector spaces of the different individual data matrices, *i.e.*, the spectral matrix, $\mathbf{S}^T$ (size $f \times w$, f refers to the number of absorbing pure component present in this complex system), is identical for each data set. Based on this premise, the augmented kinetic matrix of size $(t \times m) \times f$, $\mathbf{C}_{aug}$, and the spectral matrix, $\mathbf{S}^T$, can be extracted from the original augmented matrix, $\mathbf{D}_{aug}$, using the MCR-ALS algorithm. Concurrently, an augmented residual matrix of size $(t \times m) \times w$, $\mathbf{E}_{aug}$, is obtained. The augmented kinetic matrix, $\mathbf{C}_{aug}$, is split to m submatrices of size $t \times f$, $\mathbf{C}_1$, $\mathbf{C}_2$, $\mathbf{C}_3 \ldots \mathbf{C}_m$, containing kinetic profiles of f absorbing pure components. The m submatrices are then organized to a new matrix of size $t \times (m \times f)$ along the f dimension. Finally, the concentration data at the temporal endpoint in this new matrix are chosen to give the distribution diagram of f absorbing pure components.

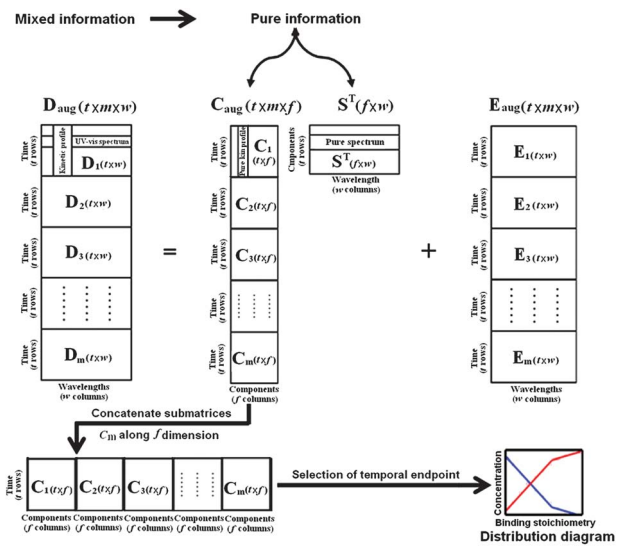

Scheme 1 Application of MCR-ALS algorithm to several time-dependent UV-visible spectra data of protein–nanomaterial conjugate. Resolution of MCR-ALS for a column-wise augmented data matrix, $\mathbf{D}_{aug}$, which is composed of m time-dependent spectral data matrix ($\mathbf{D}_1$, $\mathbf{D}_2$, $\mathbf{D}_3 \ldots \mathbf{D}_m$) related to mole-ratio experiments. $\mathbf{C}_{aug}$ denotes the augmented kinetic matrix of absorbing pure species that can be rearranged to n small kinetic matrix ($\mathbf{C}_1$, $\mathbf{C}_2$, $\mathbf{C}_3 \ldots \mathbf{C}_m$). $\mathbf{S}^T$ and $\mathbf{E}_{aug}$ are the spectral matrix of absorbing pure species and the augmented residual matrix, respectively.

Results and discussion

UV-visible spectral and kinetic characteristics of AgNPs–HSA conjugate

Time-dependent UV-visible absorption spectra of citrate-coated AgNPs in the absence or presence of increasing concentration of HSA were measured at 298.15 K (Fig. 1). As shown in Fig. 1A, the citrate-coated AgNPs possess a strong absorption band peaking at 412 nm. After HSA was added to the citrate-coated AgNPs, the maximum absorbance of the AgNPs increased gradually with a

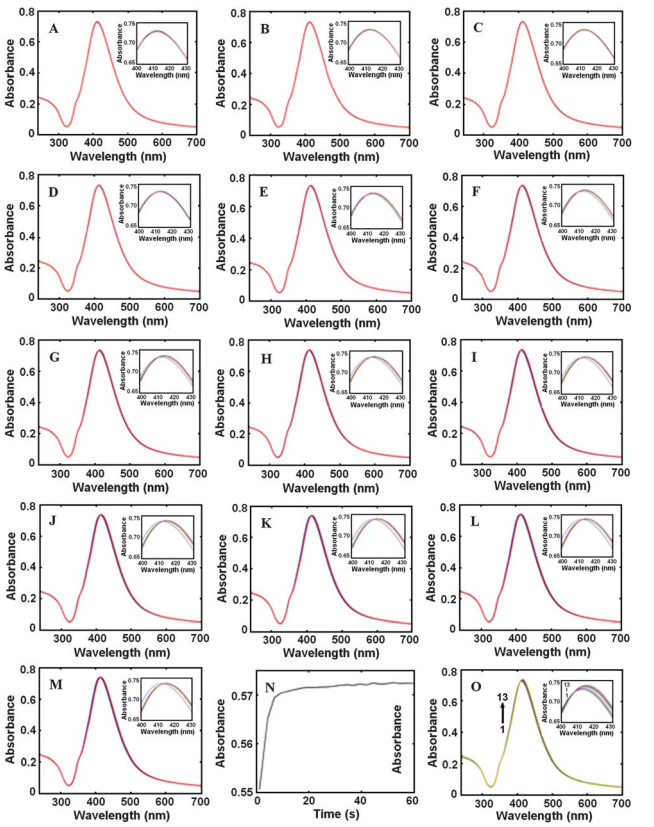

Fig. 1 Time-dependent UV-visible spectra of 0.0221 nM AgNPs at 298.15 K with different concentrations (nM) of HSA, (A) 0, (B) 1.9, (C) 3.8, (D) 7.5, (E) 15.0, (F) 22.5, (G) 30.0, (H) 37.5, (I) 45.0, (J) 52.5, (K) 60.0, (L) 67.5, (M) 75.0. (N) Kinetic curve at 445 nm under the experimental conditions in (M). (O) UV-visible spectra at temporal endpoint extracted from (A–M). Arrow shows spectra with increasing HSA concentration. Inset: enlarged spectra from 400 nm to 430 nm.

very small red-shift of the absorption peak (around 1–3 nm) and a slight broadening of the absorption spectra in long-wavelength range (Fig. 1B–M). Fig. 1N displays that upon the addition of HSA, the system achieved a steady state at around 20 s. In addition, we extracted the UV-visible spectra at the end of the reaction from the raw time-dependent spectra (Fig. 1O). It is clear in Fig. 1O that with the increase of HSA concentration, a broadening of the absorption spectra can be observed, combined with an enhancement in the absorption and a red-shift of the absorption peak. All these strongly imply that HSA was attached to the AgNPs surface to give a stable AgNPs–HSA conjugate.

Characterization of TEM, CD and FT-IR for AgNPs–HSA conjugate

To verify the interpretations given by UV-visible absorption spectra, three complementary characterization techniques, namely TEM, CD and FT-IR, were further carried out to analyse the AgNPs–HSA conjugate. As can be clearly seen from the TEM image of AgNPs in the presence of HSA (Fig. 2A), AgNPs remain nearly spherical particles and well dispersed. In addition, we can observe from Fig. 2A that AgNPs surrounded by HSA form a core (AgNPs)–shell (HSA)-type structure, showing the presence of AgNPs–HSA conjugate.

Fig. 2B shows CD spectra of AgNPs, HSA and their combination. As can be noted, AgNPs present no CD activity. And HSA exhibits two representative negative bands in the ultraviolet region at 208 nm and 220 nm, which are assigned to the α-helix structure of the protein.[45] The addition of AgNPs to HSA led to a remarkable decrease in ellipticity of the band around 208 nm. The result denotes the structural alteration from α-helix conformation to β-sheet conformation, which is in good agreement with IR results.

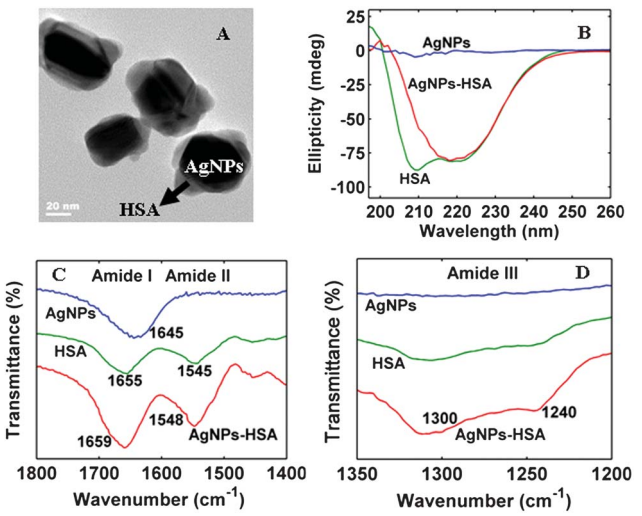

Fig. 2 (A) TEM image of AgNPs in the presence of HSA. (B) CD spectra of HSA and citrate-coated AgNPs (0.0210 nM) in the absence or presence of HSA (8.4 μM). Comparison of Fourier transform infrared spectra of HSA (459 μM) and citrate-capped AgNPs (0.002 nM) with and without HSA: (C) amide I and amide II regions; (B) amide III region.

The FT-IR investigations of HSA in the absence or presence of AgNPs were performed with the amide I (1600–1700 cm^{-1}), amide II (1500–1600 cm^{-1}) and amide III bands (1350–1200 cm^{-1}) (Fig. 2C and D). The bands around 1655 cm^{-1} and 1545 cm^{-1} can be observed for free HSA (Fig. 2C). Both of the IR peaks can be assigned to the C=O stretching, and coupling between C–N stretching and N–H bending modes, respectively.[46–48] In addition, a peak around 1645 cm^{-1} can be observed for the citrate-capped AgNPs (Fig. 2C), which originate from carboxylate asymmetric stretching vibration of citrate on the AgNPs surface.[49] After the addition of AgNPs, the peak position of the amide I and amide II bands in HSA spectra shifted up to 1659 cm^{-1} and to 1548 cm^{-1}, respectively, indicating the structural change of HSA from a significant α-helix structure to a less compact structure and the presence of citrate on the AgNPs surface.[46–48] Moreover, the blue-shift in amide II band implies the presence of many hydrogen bonds affecting N–H bending vibrations.[47] Based on the IR results, we suppose that HSA molecules are very likely to be associated with AgNPs surface to form a stable AgNPs–HSA conjugate and the binding process takes place mainly through interactions between the positively charged amino acid residues ($–NH_2$) of HSA and the negatively charged carboxyl group (–COOH) of citrate on the AgNPs surface. The amide III band of HSA is also assigned to the coupling between C–N stretching and N–H bending mode.[48] It can be observed in Fig. 2D that a broad band around 1300 cm^{-1} appears in the presence of HSA, which is attributed to the α-helix.[46,47] AgNPs have no IR activity in the amide III band. The addition of AgNPs to HSA results in the appearance of a new band around 1240 cm^{-1}, which is assigned to the β-sheet.[46,47] The structural change of HSA in the presence of AgNPs can be also reflected by the rise in the intensity ratio between 1240 cm^{-1} band and 1300 cm^{-1} band.[46,47]

Interaction study between HSA and AgNPs by time-dependent UV-visible spectra and MCR-ALS

To study the interaction mechanism between HSA and AgNPs, we introduced the MCR-ALS tool to extract kinetic and thermodynamic information from traditional UV-visible spectroscopy quantitatively. Firstly, we analysed the time-dependent UV-visible absorption spectra of citrate-coated AgNPs with thirteen different concentrations of HSA at three temperatures (298.15 K, 303.15 K and 308.15 K) (Fig. 1, S2 and S3†). The number of the absorbing pure species at three temperatures can be assessed by error theory in factor analysis, respectively.[44] Because almost no absorption appeared for the complex evolving system in the 600–700 nm wavelength region, we took the greatest contributions in the wavelength region as the noise level. The kinetic-spectral data at different temperatures were analysed by principal factor analysis, and the results denote that the Malinowski's real error (RE) given by the second abstract factor at three temperatures was lower than their respective expected noise level, suggesting no severe deviations from linearity in the experimental data and the validity of the assumption of experimental data to conform to a bilinear structure. These results show that the same two (common)

major absorbing species were involved in the complex evolving system. We consider that both of the absorbing species are AgNPs and AgNPs–HSA conjugate, respectively. Herein, we excluded the optical contribution of HSA to the absorption spectra, because HSA almost gives no measurable absorbance based on its molar extinction coefficient and the concentration used in this study. The idea was confirmed by Fig. S4.† In addition, it needs to be emphasized that because HSA may possess multiple active sites which can be absorbed or attached to the AgNPs surface, the AgNPs–HSA conjugate should not simply be interpreted as a single specific complex but as an average of a complex mixture related to the AgNPs–HSA binding.

Evolving factor analysis (EFA) was then applied to the column-wise augmented data matrix consisting of the thirteen experimental data sets at different temperatures to estimate the initial concentrations, and the estimated concentrations, which are related to the two species, and which were continually optimized by the MCR-ALS model. Simultaneously, MCR-ALS was used to force all the kinetic profiles and spectra to be non-negative according to the intrinsic properties of kinetics and spectra. The constraint of correspondence of species was employed by setting a null kinetic profile of AgNPs–HSA conjugate in pure AgNPs experiment. Closure constraint for the system was applied to the kinetic profile of HSA and AgNPs–HSA conjugate because the total concentration of HSA remained unchangeable.

The MCR-ALS resolved kinetic profiles and spectra at different temperature were displayed in Fig. 3A–C, S5A–C and S6A–C.† The lack of fit and the variance explained were below 0.38% and 99.99%, respectively, denoting that the resolution results were reliable. Looking at the kinetic profiles of HSA and AgNPs–HSA conjugate (Fig. 3, S5 and S6 in ESI†), it can be observed that as the reaction between HSA and AgNPs proceeded, the concentrations of AgNPs declined exponentially, while those of AgNPs–HSA conjugate grew exponentially. Moreover, with the increase of the added HSA concentration, the extent of concentration change for HSA and AgNPs–HSA conjugate gradually increased. Following a pseudo-first-order kinetics, the reaction rate constants at 298.15 K, 303.15 K and 308.15 K can be estimated to be 2.1×10^{-4} s^{-1}, 2.1×10^{-4} s^{-1} and 2.4×10^{-4} s^{-1}, respectively. The true spectra of AgNPs coincided closely with the resolved spectra of AgNPs with a similarity coefficient of 0.9999 (Fig. 3C, S5C and S6C†) further confirming the validity of all resolutions. Compared with AgNPs, the absorption band of the AgNPs–HSA conjugate intensified, broadened, and red shifted from 412 nm to 415 nm (Fig. 3C), and the molar extinction coefficient of the AgNPs–HSA conjugate was calculated to be 3.35×10^{10} M^{-1} cm^{-1} at absorbance maximum, about 1.01-fold larger than that of citrate-coated AgNPs. Noticeably, although only very weak spectral variations are obtained at different concentrations of HSA in the presence of AgNPs, good resolution results were still achieved. We suppose that several sets of time-dependent spectral data are analyzed simultaneously, increase the information on the chemical phenomena, and as a result reduce the rotational ambiguity of spectral resolution.

To obtain the distribution diagram of AgNPs and AgNPs–HSA conjugate at equilibrium, we extracted the concentration at temporal endpoint from their respective kinetic profiles (Fig. 3D, S5D and S6D†). The distribution diagram clearly shows that there was a considerable decrease in the AgNPs concentration, accompanied by an apparent increase in the concentration of AgNPs–HSA conjugate. The molar binding ratio of HSA to AgNPs can be calculated from the abscissa of the intersection point of the two tangents drawn to the initial and final parts of the concentration evolution of the AgNPs and AgNPs–HSA conjugate. It was found that the molar binding ratio between HSA and AgNPs at three temperatures was about 2.1×10^3. From the MCR-ALS estimated distribution diagrams, the apparent binding constant, K_{app}, of the AgNPs–HSA conjugate is likely to be conveniently calculated based on the following equation:

$$K_{app} = \frac{[\text{AgNPs} - \text{HSA}]}{[\text{AgNPs}][\text{HSA}]} \quad (5)$$

where [AgNPs–HSA], [AgNPs] and [HSA] represent the estimated equilibrium concentrations of AgNPs–HSA conjugate, AgNPs and HSA, respectively.

The apparent binding constant at 298.15 K, 303.15 K and 308.15 K can be estimated to be 1.29 nM^{-1}, 2.89 nM^{-1} and 1.25 nM^{-1}, respectively. Assuming that the enthalpy change (ΔH) do not change significantly over the temperature range studied, three thermodynamic parameters related to the interaction of HSA and AgNPs, standard enthalpy change (ΔH), standard entropy change (ΔS) and standard Gibbs free energy change (ΔG), can be determined using the equation below:[50,51]

$$\ln K_{app} = -\frac{\Delta H}{RT} + \frac{\Delta S}{R} \quad (6)$$

$$\Delta G = \Delta H - T\Delta S = -RT \ln K_{app} \quad (7)$$

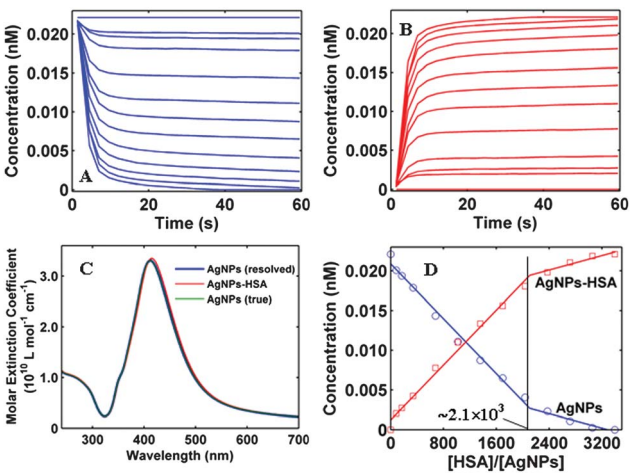

Fig. 3 MCR-ALS resolved kinetic curves of AgNPs (A) and AgNPs–HSA conjugate (B) at 298.15 K. (C) Resolved spectra of AgNPs and AgNPs–HSA conjugate and the true pure spectra of AgNPs. (D) Resolved distribution diagrams of AgNPs and AgNPs–HSA conjugate.

where R and T denote the gas constant and the thermodynamic temperature, respectively. The value of ΔG is determined by eqn (7). The value of ΔH and ΔS can be estimated from the linear relationship between $\ln K_{app}$ and the reciprocal a thermodynamic temperature ($1/T$).

According to the binding constants at the three temperatures above, the ΔG values at 298.15 K, 303.15 K and 308.15 K are calculated to be -52.0 kJ mol^{-1}, -54.9 kJ mol^{-1} and -53.7 kJ mol^{-1}, respectively.The values of ΔH and ΔS are estimated to be -2.0 kJ mol^{-1} and 169.9 J mol^{-1} K^{-1}, respectively. Based on the relationship between the sign of the three thermodynamic parameters and various molecular forces, we suppose that the electrostatic interaction between the positively amino acid residues of HSA and the negatively carboxyl group of citrate on the AgNPs surface may play a major role in the binding process of HSA to AgNPs and result in the stability of the bionanoconjugate, which is substantially consistent with the above IR results.

In addition, the MCR-ALS resolved results were further used to delineate the structure of HSA on the AgNPs surface. The actually average projected surface area per HSA molecule on AgNP, named as the molecular footprint, can be calculated by dividing the total surface area per AgNP by the binding stoichiometry between HSA and AgNPs. According to the diameter (38.6 nm) of the bare AgNP measured from TEM, the radius and the total surface area per AgNP are estimated to be 19.3 nm and 4681 nm^2 ($4 \times \pi \times 19.3^2$ nm^2), respectively. Based on the binding stoichiometry deduced above, the actually saturated surface area per HSA molecule on AgNP can be calculated to be 2.2 nm^2. Earlier literature has reported a triangular prism-shaped structure of serum albumin in solution with sides of 8.4 nm and a height of 3.15 nm.[40] Based on the known HSA model, the theoretically surface area per HSA molecule on AgNP surface in a "flat-on" or "end-on" conformation are near to 30.6 nm^2 ($1/2 \times 8.4^2 \times \sin(\pi/3)$ nm^2) and 26.5 nm^2 (3.15×8.4 nm^2), respectively. The theoretical surface area values for the two conformations of HSA are far greater than the actual saturated surface area value, implying that HSA is very likely attached to the AgNPs surface mainly in the form of a multilayer. The multilayer arrangement of HSA reveals the presence of "hard" and "soft" protein corona on the AgNPs surface. Moreover, according to the previously proposed method,[52] the theoretically saturated number, N, of the bound protein molecules for a monolayer coverage on a spherical nanoparticle can be calculated as:

$$N = \left[\left(\frac{R_N}{R_0}\right)^3 - 1\right] \times \frac{V_0}{V_p} \quad (8)$$

where V_p, V_0, R_N and R_0 are the volume of the bound protein molecule, the volume of nanoparticle without protein, and the radii of nanoparticle with and without protein.

The HSA molecule has a volume of 96.3 nm^3 ($3.15 \times 1/2 \times 8.42 \times \sin(\pi/3)$ nm^3) and the volume of AgNPs is calculated to be 30 113 nm^3 ($4/3 \times \pi \times 19.3^3$ nm^3). When the HSA molecule is attached to the AgNPs surface in a "flat-on" or "end-on" conformation, the radius of AgNPs–HSA conjugate approximates to 22.45 nm (19.3 + 3.15 nm) and 26.57 nm (19.3 + 8.4 × $\sin(\pi/3)$ nm), respectively. Hence, for a complete surface monolayer coverage, the theoretically saturated number of HSA molecules attached per AgNP is approximately equal to about 180 and 504, respectively. The two values are much lower than the above actual saturated number (2.1×10^3), further demonstrating the multilayer structure of HSA attached to AgNPs surface.

Spectroscopic biosensor for detection of HSA

Concurrent with our study of protein–nanomaterial interaction, we fabricated a sensitive spectroscopic biosensor for HSA using a MCR-ALS resolved concentration evolution in Fig. 3D. It was found that the resolved concentration of AgNPs or AgNPs–HSA conjugate was linear with the added concentration of HSA over a range from 1.9 nM to 45.0 nM. The linear regression equations for AgNPs and AgNPs–HSA conjugate were c_{AgNPs} (nM) $= -3.8 \times 10^{-4} c_{HSA}$ (nM) + 0.020 (correlation coefficient $r = 0.997$) and $c_{HSA-AgNPs}$ (nM) $= 3.8 \times 10^{-4} c_{HSA}$ (nM) + 0.002 (correlation coefficient $r = 0.997$), respectively. Detection limits with a signal-to-noise ratio (S/N) of 3 was determined to be 0.9 nM for both AgNPs and AgNPs–HSA conjugate calibrations, which compared well with those values given by sensitive fluorometric methods.[48,53,54]

Conclusions

The interaction between HSA and AgNPs was studied in detail for the first time with time-dependent UV-visible spectroscopy coupled with MCR-ALS algorithm. The formation of AgNPs–HSA conjugate can be readily confirmed by observing variations of absorption spectra. The application of the MCR-ALS tool in the complex evolving system gave a new insight into the HSA–AgNPs interaction, allowing quantitative recovery of the kinetic profiles, spectra and distribution diagrams of the absorbing pure species (AgNPs and AgNPs–HSA conjugate). The response profiles can provide kinetic, thermodynamic and structural information about the evolution of AgNPs–HSA conjugate. The obtained information can further give a possible explanation of the action force and arrangement of HSA binding to the AgNPs surface.

Moreover, TEM, CD and FT-IR were employed to investigate the AgNPs–HSA conjugate. The results given by three complementary characterization techniques demonstrated the validity of the proposed method for the study of the AgNPs–HSA conjugate. Concurrently, the MCR-ALS resolved concentrations of the spectroscopically active pure species were exploited to construct a biosensor for the sensitive detection of HSA. The nanobiosensor in our study exhibited almost no selectivity for HSA, but the second-order advantage from the kinetic-spectral data matrices[55–57] can partially or entirely make up for its deficiency.

The example presented in this work is a case study of protein–nanomaterial interactions that clearly demonstrates all the benefits of the combination of UV-visible spectroscopy and the MCR-ALS tool. The method proposed opens a new stage for future investigations utilizing the mechanistic understanding

of protein–nanomaterial interactions and the mode of action of these bionanoconjugates to assess their performance in relation to bioanalytical chemistry, biosensor, biocatalysis, biofuel cells and bio-based nanodevices in a more systematic fashion. The information obtained from the method will possibly be a basis for screening and engineering nanomaterials with appropriate ligand functionality and proteins with a specific property. It needs to be emphasized that the proposed method is, by no means, limited to routine UV-visible spectroscopy and can be extended to other various analytical techniques, such as fluorescence, chromatography, electrochemistry and so on. It is believed that these techniques coupled with a chemometrics tool will give much richer information on protein–nanomaterial interaction like binding mode, binding sites and so on. More importantly, the implicit information about thermodynamics, kinetics and structure of protein attachment onto nanomaterials, which is extracted by the MCR-ALS tool, may provide a theoretical guide for the fabrication and optimization of a robust nanobiosensor or cross-reactive sensors array for the detection and identification of biocomponents. This work may also open the door for the development and application of more new chemometrics models in the fields of bionanotechnology. Many studies to this end are currently underway.

Acknowledgements

This work was supported by the National Natural Science Foundation of China (NSFC-21065007 and NSFC-21305061), the Natural Science Foundation of Jiangxi Province (20132BAB213011), the Jiangxi Provincial Department of Education (GJJ13026) and the State Key Laboratory of Food Science and Technology of Nanchang University (SKLF-ZZA-201302 and SKLF-ZZB-201303).

Notes and references

1 M. Sarikaya, C. Tamerler, A. K. Y. Jen, K. Schulten and F. Baneyx, *Nat. Mater.*, 2013, **85**, 2143.
2 Z. Schnepp, *Angew. Chem., Int. Ed.*, 2012, **52**, 1096.
3 A. C. Chen and S. Chatterjee, *Chem. Soc. Rev.*, 2013, **42**, 5425.
4 R. A. Sperling and W. J. Parak, *Philos. Trans. R. Soc. London, Ser. A*, 2010, **368**, 1333.
5 Q. Huo, *Colloids Surf., B*, 2007, **59**, 1.
6 C. C. You, A. Verma and V. M. Rotello, *Soft Matter*, 2006, **2**, 190.
7 E. Buxbaum, *Fundamentals of Protein Structure and Function*, Springer-Verlag, New York, 2007.
8 J. Bao, W. Che, T. T. Liu, Y. L. Zhu, P. Y. Jin, L. Y. Wang, J. F. Liu, Y. G. Wei and Y. D. Li, *ACS Nano*, 2007, **1**, 293.
9 B. Y. Wu, H. F. Wang, J. T. Chen and X. P. Yan, *J. Am. Chem. Soc.*, 2011, **133**, 686.
10 L. N. Feng, Z. P. Bian, J. Peng, F. Jiang, G. H. Yang, Y. D. Zhu, D. Yang, L. P. Jiang and J. J. Zhu, *Anal. Chem.*, 2012, **84**, 7810.
11 J. M. Liu, J. T. Chen and X. P. Yan, *Anal. Chem.*, 2013, **85**, 3238.
12 J. T. La Belle, A. Fairchild, U. K. Demirok and A. Verma, *Methods*, 2013, **61**, 39.
13 P. Wu, Y. He, H. F. Wang and X. P. Yan, *Anal. Chem.*, 2010, **82**, 1427.
14 M. J. Ruedas-Rama and E. A. H. Hall, *Anal. Chem.*, 2010, **82**, 9043.
15 I. Ron, I. Pecht, M. Sheves and D. Cahen, *Acc. Chem. Res.*, 2010, **43**, 945.
16 N. Solin and O. Inganas, *Isr. J. Chem.*, 2012, **52**, 529.
17 M. Rahman, S. Laurent, N. Tawil, L. Yahia and M. Mahmoudi, *Protein–Nanoparticle Interactions: The Bio-Nano Interface*, Springer-Verlag, New York, 2013.
18 H. Jans, X. Liu, L. Austin, G. Maes and Q. Huo, *Anal. Chem.*, 2009, **81**, 9425.
19 M. E. Aubin-Tam and K. Hamad-Schifferli, *Biomed. Mater.*, 2008, **3**, 034001.
20 K. E. Sapsford, K. M. Tyner, B. J. Dair, J. R. Deschamps and I. L. Medintz, *Anal. Chem.*, 2011, **83**, 4453.
21 L. W. Li, Q. X. Mu, B. Zhang and B. Yan, *Analyst*, 2010, **135**, 1519.
22 I. Delfino and S. Cannistraro, *Biophys. Chem.*, 2009, **139**, 1.
23 J. Deka, A. Paul and A. Chattopadhyay, *J. Phys. Chem. C*, 2009, **113**, 6936.
24 J. J. Mueller, S. Baum, L. Hilterhaus, M. Eckstein, O. Thum and A. Liese, *Anal. Chem.*, 2013, **83**, 9321.
25 H. B. Liu, X. L. Yang, L. Liu, J. Z. Dang, Y. L. Xie, Y. Zhang, J. Pu, G. B. Long, Y. L. Li, Y. H. Yuan, J. Liao and F. Liao, *Anal. Chem.*, 2013, **85**, 2143.
26 E. Edri and O. Regev, *Anal. Chem.*, 2008, **80**, 4049.
27 J. Irrgang, J. Ksienczyk, V. Lapiene and C. M. Niemeyer, *ChemPhysChem*, 2009, **10**, 1483.
28 Y. Akhlaghi, M. Kompany-Zareh and M. R. Hormozi-Nezhad, *Anal. Chem.*, 2012, **84**, 6603.
29 S. Gholami and M. Kompany-Zareh, *Phys. Chem. Chem. Phys.*, 2013, **15**, 14405.
30 S. Gholami and M. Kompany-Zareh, *Anal. Bioanal. Chem.*, 2013, **405**, 6271.
31 H. Kong, Y. X. Lu, H. Wang, F. Wen, S. C. Zhang and X. R. Zhang, *Anal. Chem.*, 2012, **84**, 4258.
32 J. Jaumot, R. Gargallo, A. De Juan and R. Tauler, *Chemom. Intell. Lab. Syst.*, 2005, **76**, 101.
33 R. D. JiJi, G. G. Andersson and K. S. Booksh, *J. Chemom.*, 2000, **14**, 171.
34 P. Cutler, P. J. Gemperline and A. De Juan, *Anal. Chim. Acta*, 2009, **632**, 52.
35 I. Marti-Aluja, I. Ruisanchez and M. Soledad Larrechi, *Anal. Chim. Acta*, 2013, **760**, 16.
36 K. Wongravee, T. Parnklang, P. Pienpinijtham, C. Lertvachirapaiboon, Y. Ozaki, C. Thammacharoen and S. Ekgasit, *Phys. Chem. Chem. Phys.*, 2013, **15**, 4183.
37 B. Hemmateenejad and M. R. H. Nezhad, *J. Phys. Chem. C*, 2008, **112**, 18321.
38 S. Chernousova and M. Epple, *Angew. Chem., Int. Ed.*, 2013, **52**, 1636.
39 Z. H. Huang, X. L. Jiang, D. W. Guo and N. Gu, *J. Nanosci. Nanotechnol.*, 2011, **11**, 9395.
40 X. M. He and D. C. Carter, *Nature*, 1992, **358**, 209.
41 T. Peters, *All about Albumins: Biochemistry, Genetics and Medical Applications*, Academic Press, San Diego, 1996.

42 P. C. Lee and D. Meisel, *J. Phys. Chem.*, 1982, **86**, 3391.
43 R. Kanjanawarut and X. D. Su, *Anal. Chem.*, 2009, **81**, 6122.
44 E. R. Malinowski, M. J. Barber, G. T. Whitaker and E. T. Smith, *J. Chemom.*, 2007, **21**, 520.
45 Y. N. Hong, C. Feng, Y. Yu, J. Z. Liu, J. W. Y. Lam, K. Q. Luo and B. Z. Tang, *Anal. Chem.*, 2010, **82**, 7035.
46 T. J. Lenk, B. D. Ratner, R. M. Gendreau and K. K. Chittur, *J. Biomed. Mater. Res.*, 1989, **23**, 549.
47 K. Kaiden, T. Matsui and S. Tanaka, *Appl. Spectrosc.*, 1987, **41**, 180.
48 J. L. Kong and S. N. S. Yu, *Acta Biochim. Biophys. Sin.*, 2007, **39**, 549.
49 P. Wulandari, X. H. Li, K. Tamada and M. J. Hara, *J. Nonlinear Opt. Phys. Mater.*, 2008, **17**, 185.
50 P. Atkins and J. De Paula, *Physical Chemistry*, W. H. Freeman and Company, New York, 2006.
51 T. M. Lovestead and T. J. Bruno, *Anal. Chem.*, 2010, **82**, 5621.
52 C. Rocker, M. Potzl, F. Zhang, W. J. Parak and G. U. Nienhaus, *Nat. Nanotechnol.*, 2009, **4**, 577.
53 X. H. Wang, X. Y. Wang, Y. Q. Wang and Z. J. Guo, *Chem. Commun.*, 2011, **47**, 8127.
54 Y. H. Ahn, J. S. Lee and Y. T. Chang, *J. Comb. Chem.*, 2008, **10**, 376.
55 A. Espionosa-Mansilla, A. M. De La Pena, T. C. Goicoechea and A. C. Oliveri, *Appl. Spectrosc.*, 2004, **58**, 83.
56 P. Pasamontes and M. P. Callao, *Trends Anal. Chem.*, 2006, **25**, 77.
57 S. A. Bortolato, J. A. Arancibia and G. M. Escandar, *Anal. Chem.*, 2009, **81**, 8074.